JACS Au
AN OPEN ACCESS JOURNAL OF THE AMERICAN CHEMICAL SOCIETY

pubs.acs.org/jacsau

Article

Simultaneously Achieving Fast Intramolecular Charge Transfer and Mass Transport in Holey D−π−A Organic Conjugated Polymers for Highly Efficient Photocatalytic Pollutant Degradation

Huinan Che, Jian Wang, Peifang Wang, Yanhui Ao,* Juan Chen, Xin Gao, Fangyuan Zhu, and Bin Liu*

Cite This: *JACS Au* 2023, 3, 1424−1434

Read Online

ACCESS | Metrics & More | Article Recommendations | Supporting Information

ABSTRACT: Simultaneously realizing efficient intramolecular charge transfer and mass transport in metal-free polymer photocatalysts is critical but challenging for environmental remediation. Herein, we develop a simple strategy to construct holey polymeric carbon nitride (PCN)-based donor−π−acceptor organic conjugated polymers via copolymerizing urea with 5-bromo-2-thiophenecarboxaldehyde (PCN−5B2T D−π−A OCPs). The resultant PCN−5B2T D−π−A OCPs extended the π-conjugate structure and introduced abundant micro-, meso-, and macro-pores, which greatly promoted intramolecular charge transfer, light absorption, and mass transport and thus significantly enhanced the photocatalytic performance in pollutant degradation. The apparent rate constant of the optimized PCN−5B2T D−π−A OCP for 2-mercaptobenzothiazole (2-MBT) removal is ∼10 times higher than that of the pure PCN. Density functional theory calculations reveal that the photogenerated electrons in PCN−5B2T D−π−A OCPs are much easier to transfer from the donor tertiary amine group to the benzene π-bridge and then to the acceptor imine group, while 2-MBT is more easily adsorbed on π-bridge and reacts with the photogenerated holes. A Fukui function calculation on the intermediates of 2-MBT predicted the real-time changing of actual reaction sites during the entire degradation process. Additionally, computational fluid dynamics further verified the rapid mass transport in holey PCN−5B2T D−π−A OCPs. These results demonstrate a novel concept toward highly efficient photocatalysis for environmental remediation by improving both intramolecular charge transfer and mass transport.

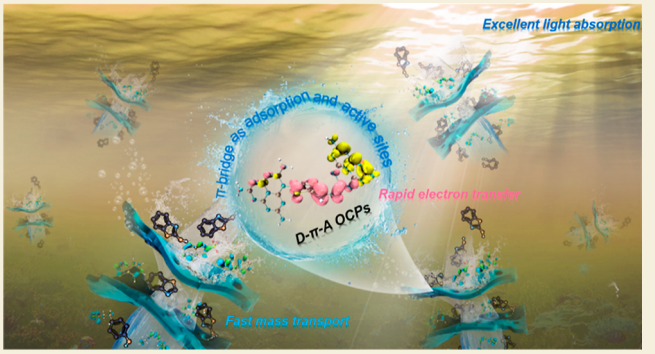

KEYWORDS: *intramolecular charge transfer, mass transport, organic conjugated polymers, pollutant degradation, holey structure*

INTRODUCTION

Photocatalytic degradation, which possesses the characteristics of environmental friendliness, simplicity of operation, and mild reaction conditions, is becoming a prospective strategy for solving the problem of water pollution.[1−3] Generally, an ideal photocatalyst for high-efficiency photocatalytic degradation reactions should possess an appropriate band structure, good chemical stability, favorable surface adsorption properties, and a simple synthesis method. Noticeably, polymeric carbon nitride (PCN), as a typical metal-free semiconductor, has attracted ever-increasing attention for photocatalytic wastewater treatment.[4−6] The N-bridged heptazine ring structure of PCN ensures its high structural stability, and the π-conjugated electronic structure to some extent accelerates charge transport and separation.[7,8] Additionally, the tunable electronic structure of PCN is favorable for regulating its light absorption ability.[9,10] However, pure PCN still faces many drawbacks, including sluggish charge transfer, poor visible light absorption, and slow mass transport, which severely hinder its photocatalytic degradation performance.

To date, various strategies have been developed to tackle the issues of PCN in photocatalytic reactions, such as defect engineering,[11−14] construction of heterojunctions,[15−17] and elemental doping.[18−20] Besides, designing organic conjugated polymers (OCPs), such as donor−acceptor (D−A), A−D−A, D−A−A, D−A−D, etc., is becoming a promising strategy, and OCPs display tunable optical and electrical properties.[21] For instance, the band structure of D−A OCPs could be regulated by pushing/pulling the energy of the highest occupied molecular orbital (HOMO)/the lowest unoccupied molecular orbital (LUMO) via the D-units/A-units.[22,23] Furthermore, the D−A OCPs could effectively induce intramolecular charge transfer from D to A and thus accelerate the transport/

Received: February 20, 2023
Revised: April 21, 2023
Accepted: April 25, 2023
Published: May 6, 2023

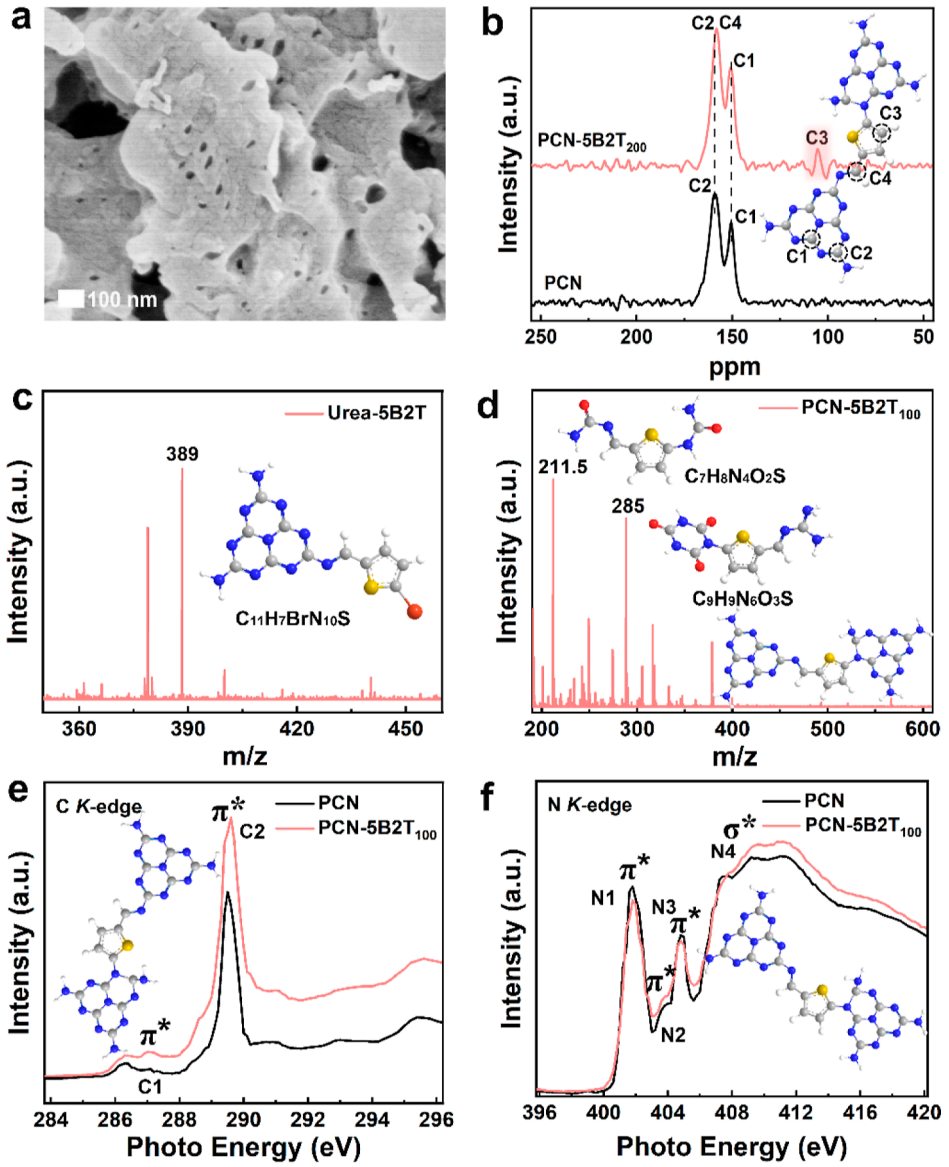

Figure 1. (a) SEM image of PCN−5B2T$_{100}$ D−π−A OCP. (b) Solid-state ^{13}C NMR spectra of PCN and PCN−5B2T$_{200}$ D−π−A OCP. (c,d) TOF-SIMS of urea-5B2T and PCN−5B2T$_{100}$ D−π−A OCP. NEXAFS profiles of PCN and TP-PCN, (e) C K-edge and (f) N K-edge.

migration of photogenerated electrons.[24−26] Although PCN-based D−A OCPs are conducive to improving charge separation, the electron delocalization in this structure is still limited, which restrains the migration of photoexcited electrons. To achieve more effective and faster intramolecular charge transfer, it is essentially necessary to induce an intrinsic driving force in the D−A for the delocalization of charge carriers around the photoexcitation sites. Fortunately, extending the π-conjugate structure is considered effective to enhance electron delocalization.[27,28] Besides, for photocatalytic degradation, light absorption and mass transport can also greatly influence photocatalytic performance. Among the various structures, the holey structure is not only conducive to promoting multiple light scattering and thus enhancing light absorption but also can effectively facilitate mass transport, both of which shall improve the photocatalytic degradation performance.[29] Additionally, early studies have calculated the Fukui function of pollutants based on density functional theory (DFT) to deduce the vulnerability of reaction sites to free radical attack; however, they are limited to the analysis of the structure of the original pollutants. It is worth noting that there is no analysis of the real-time structural change of pollutants, and the real reaction sites of intermediates will change if their structures change. Therefore, it is imperative to analyze the intermediate products of pollutant degradation in real-time to determine the actual active sites that are involved in the redox reaction.

Herein, PCN-based D−π−A OCPs with a holey structure were facilely prepared by copolymerizing urea with 5-bromo-2-thiophenecarboxaldehyde (PCN−5B2T D−π−A OCPs). The obtained PCN−5B2T$_x$ D−π−A OCPs ("x" indicates the volume (μL) of the added 5B2T) not only greatly accelerated intramolecular charge transfer but also markedly enhanced the specific surface area, light absorption, and mass transport, all of which worked synergistically to improve the photocatalytic performance of PCN−5B2T$_x$ D−π−A OCPs. As a result, the optimized PCN−5B2T$_{100}$ D−π−A OCP displayed an excellent photocatalytic degradation activity of 2-MBT with a K_{app} value of 0.299 min^{-1}, which is ∼10 times higher than that of pure PCN.

https://doi.org/10.1021/jacsau.3c00088
JACS Au 2023, 3, 1424−1434

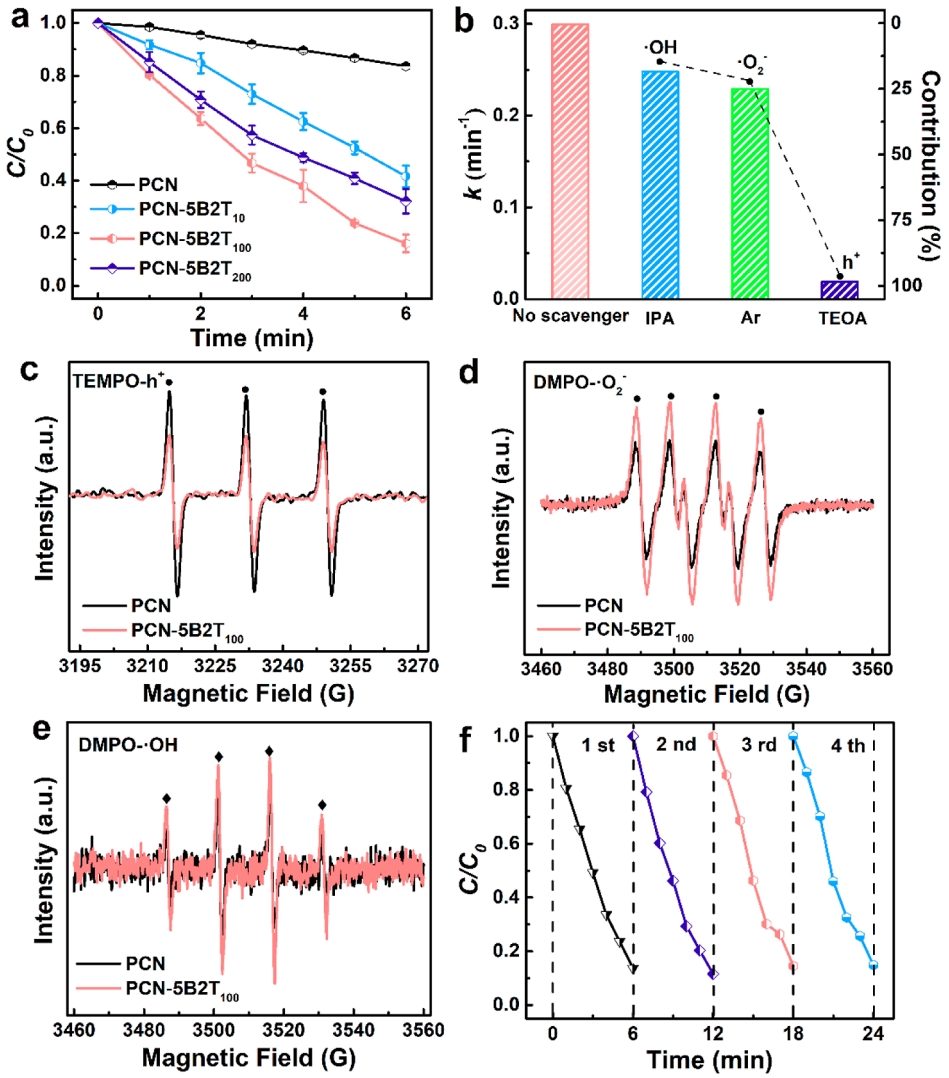

Figure 2. (a) Photocatalytic 2-MBT degradation over PCN and PCN−5B2T$_x$ D−π−A OCPs. (b) Photocatalytic degradation kinetics and the contributions of h^+, $^\bullet O_2^-$, and $^\bullet$OH for degradation of 2-MBT over PCN−5B2T$_{100}$ D−π−A OCP. ESR spectra of (c) TEMPO−h^+, (d) DMPO−$^\bullet O_2^-$, and (e) DMPO−$^\bullet$OH for PCN−5B2T$_{100}$ D−π−A OCP. (f) Cyclic photocatalytic degradation of 2-MBT over PCN−5B2T$_{100}$ D−π−A OCP.

RESULTS AND DISCUSSION

Morphology and Structure of PCN−5B2T$_x$ D−π−A OCPs

Scanning electron microscopy (SEM) and transmission electron microscopy (TEM) images show the holey nanosheet structure of PCN−5B2T$_{100}$ D−π−A OCP compared with pure PCN (Figures 1a and S1−S3). Additionally, the elemental mapping images of PCN−5B2T$_{100}$ D−π−A OCP show a uniform distribution of C, N, O, and S elements. The specific surface area (56.73 m^2/g) and pore volume (0.173 cm^3/g) of PCN−5B2T$_{100}$ D−π−A OCP are obviously increased as compared to PCN (34.86 m^2/g and pore volume: 0.143 cm^3/g, Figure S4). PCN−5B2T$_x$ D−π−A OCPs were synthesized by nucleophilic substitution and Schiff base chemical reaction through polycondensation of urea and 5B2T (Figures S5−S8). To uncover the chemical states of PCN−5B2T$_x$ D−π−A OCPs, XPS was conducted. The C 1s XPS spectra of PCN and PCN−5B2T$_{100}$ D−π−A OCP can be deconvoluted into three peaks (Figure S9a), corresponding to N−C═N (287.88 eV), C−NH$_x$ (285.93 eV), and C═C (284.53 eV).[30,31] Clearly, the peak intensity at 284.53 eV (C═C) for PCN−5B2T$_{100}$ D−π−A OCP is higher than that for PCN, indicating that 5B2T may be introduced into the framework of PCN. The N 1s XPS spectra of PCN and PCN−5B2T$_{100}$ D−π−A OCP can be resolved into four main peaks at 398.3, 399.6, 400.7, and 403.7 eV (Figure S9b), which can be assigned to C−N═C, N−(C)$_3$, C−N−H, and the charging effects, respectively.[32−35] The peak intensity of C−N═C shows an obvious decrease from PCN to PCN−5B2T$_{100}$ D−π−A OCP, which matches well with the proposed D−π−A structure. Additionally, the presence of sulfur species in PCN−5B2T$_{100}$ D−π−A OCP is verified by XPS spectra. Obviously, two characteristic peaks at 163.8 and 165.7 eV correspond to S 2p$_{1/2}$ and S 2p$_{3/2}$ (Figure S10), respectively. Note that these binding energies are very similar to the ones reported in previous works for thiophene-based molecules.[22,36,37] Additionally, the characteristic peaks at 163.7 and 164.8 eV are quite different from those (169.3 and 164.0 eV) for sulfur-doped PCN.[38] Thus, according to the S 2p XPS spectrum, we can judge that PCN−5B2T$_{100}$ D−π−A OCP is more likely recognized as a molecular doping with full thiophene groups rather than the co-doping of carbon and sulfur atoms. Besides, both PCN and PCN−5B2T$_{200}$ D−π−A

https://doi.org/10.1021/jacsau.3c00088
JACS Au 2023, 3, 1424−1434

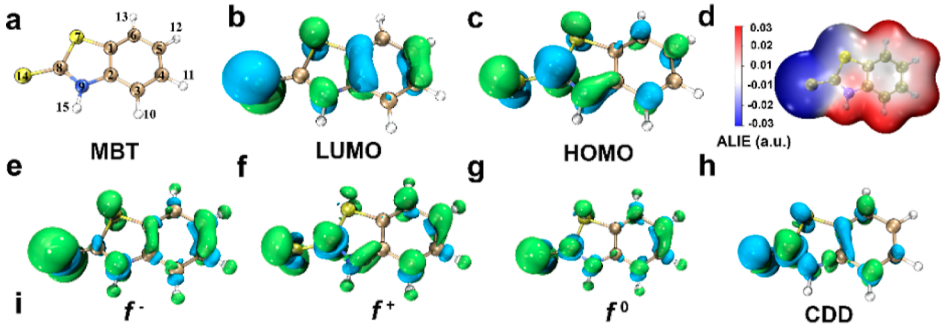

No.	Atom	Charge(-1) (e/Å^3)	Charge(0) (e/Å^3)	Charge(+1) (e/Å^3)	f^-	f^+	f^0	CDD
1	C	-0.0278	-0.0432	0.0127	0.0405	0.0154	0.0279	-0.025
2	C	0.0374	0.0097	0.0747	0.0373	0.0276	0.0325	-0.0097
3	C	-0.0502	-0.1226	-0.0145	0.0357	0.0724	0.054	0.0366
4	C	-0.0366	-0.0815	0.0222	0.0588	0.045	0.0519	-0.0138
5	C	-0.0413	-0.1124	0.0253	0.0666	0.0711	0.0689	0.0045
6	C	-0.0392	-0.1049	-0.0073	0.0319	0.0657	0.0488	0.0338
7	S	0.0832	-0.038	0.2301	0.1468	0.1212	0.134	-0.0256
8	C	0.0442	-0.0644	0.0646	0.0204	0.1086	0.0645	0.0881
9	N	-0.0463	-0.0807	0.0064	0.0527	0.0344	0.0436	-0.0183
10	H	0.051	0.0148	0.077	0.0261	0.0362	0.0311	0.0101
11	H	0.0504	0.0181	0.083	0.0326	0.0323	0.0325	-0.0003
12	H	0.0497	0.0109	0.0839	0.0341	0.0388	0.0365	0.0047
13	H	0.0548	0.0202	0.0805	0.0257	0.0346	0.0302	0.0088
14	S	-0.2856	-0.5552	0.0769	0.3625	0.2696	0.3161	-0.0928
15	H	0.1563	0.1293	0.1844	0.0281	0.0269	0.0275	-0.0012

Figure 3. (a) Optimized structure, (b) LUMO, (c) HOMO, and (d) ESP of 2-MBT. The isosurface of (e) f^-, (f) f^+, (g) f^0, and (h) CDD of 2-MBT. (i) Hirshfeld charges and calculated f^-, f^+, f^0, and CDD of 2-MBT. Yellow, blue, gray, and white represent S, N, C, and H atoms, respectively. The isosurface value is 0.004 e/Å^3.

OCP exhibit two signal peaks at 150.5 ppm (C1) and 159.4 ppm (C2), corresponding to C−NH−C and C−(N)$_3$ (Figure 1b), respectively.[39] Moreover, compared with pure PCN, new C3 peaks assignable to the incorporated aromatic carbon in the PCN network are clearly visible at approximately 105 ppm.[40] PCN−5B2T$_{200}$ D−π−A OCP possesses a new characteristic peak at 157.1 ppm (Figure S11), which can be attributed to the carbon atoms of imine units.[41] All these results confirm that the PCN−5B2T$_x$ D−π−A OCPs were successfully synthesized by nucleophilic substitution and Schiff base chemical reactions through polycondensation of urea and 5B2T. In addition, matrix-assisted laser desorption ionization-time of flight mass (MALDI−TOF MS) spectroscopy further confirms the formation of the PCN−5B2T$_x$ D−π−A OCPs structure. Notably, an obvious peak (m/z = 389) could be observed in the MS spectrum of urea-5B2T (Figure 1c), indicating that $C_{11}H_7BrN_{10}S$ was produced by the Schiff base chemical reaction. In addition, two peaks (m/z = 236 and m/z = 330) were observed in the case of PCN−5B2T$_{100}$ (300 °C) D−π−A OCP, which can be assigned to $C_8H_{10}N_6OS$ and $C_{11}H_{10}N_{10}OS$ (Figure S12). These results further indicate that the intermediates of $C_8H_{10}N_6OS$ and $C_{11}H_{10}N_{10}OS$ are formed by nucleophilic substitution. Most importantly, the peaks with m/z of 212, 281, and 400−500 can be observed in the MALDI−TOF MS spectrum of PCN−5B2T$_{100}$ (550 °C) D−π−A OCP, corresponding to $C_7H_8N_4O_2S$, $C_9H_9N_6O_3S$, and PCN−5B2T$_{100}$ D−π−A OCP, respectively (Figure 1d). Relevant structural characteristics of PCN−5B2T$_{100}$ D−π−A OCPs are further investigated by C and N K-edge XANES measurement (Figure 1e,f). Obviously, in the C K-edge XANES spectra (Figure 1e), both samples show a typical structure of PCN, which can be attributed to π^* (C1, C−C/C═C) and π^* (C2, C−N−C), respectively. Interestingly, the intensity of π^* (C−C/C═C) for PCN−5B2T$_{100}$ D−π−A OCP is higher than that for PCN, which may be derived from the introduction of π-conjugation.[42] The peak intensity of π^* (C−N−C) also enhances after the incorporation of 5B2T into the conjugated network of PCN, indicating a stronger interfacial interaction between π-bridge units and the basal plane of PCN. Such stronger interfacial interaction can accelerate the electron transport in PCN−5B2T$_x$ D−π−A OCPs, which brings efficient charge separation/transfer.[27] In addition, in the N K-edge XANES spectra (Figure 1f), PCN and PCN−5B2T$_{100}$ D−π−A OCP display four peaks, which can be assigned to π^* (N1, C−N−C), π^* (N2, N−C$_3$ bridging), π^* (N3, N−C$_3$), and σ^* (N4, C−N−C/C−N). The enhancement of π^* (N3, N−C$_3$ bridging) feature for PCN−5B2T$_{100}$ D−π−A OCP indicated a strengthened interfacial interaction between π-bridge units and the basal plane of PCN, which is consistent with the result of the C K-edge XANES spectra.

https://doi.org/10.1021/jacsau.3c00088
JACS Au 2023, 3, 1424−1434

Highly Efficient Photocatalytic Activity by the Construction of D−π−A OCPs

The photocatalytic activities of as-prepared samples were evaluated by the degradation of 2-MBT under visible light irradiation. Figure S13 shows that all of the samples could reach adsorption−desorption equilibrium in the dark in 30 min. Strikingly, all PCN−5B2T$_x$ D−π−A OCPs show significantly enhanced photocatalytic 2-MBT degradation activities than PCN (Figures 2a, S14, and S15). Especially, PCN−5B2T$_{100}$ D−π−A OCP has the highest photodegradation rate constant (K_{app}, 0.299 min^{-1}), which is about 9.97 times that for pure PCN (Figure S15a). The photocatalytic degradation activity of 2-MBT under different environments reveals that PCN−5B2T$_x$ D−π−A OCPs has excellent practical application potential (Figure S15b−d). To further examine the photodegradation mechanism, photocatalytic 2-MBT degradation was carried out in the presence of different scavengers (Figure S16). Remarkably, the photocatalytic degradation efficiency was greatly decreased with the addition of triethanolamine (TEOA), indicating that photogenerated h$^+$ might be the main reactive species. Oppositely, the addition of isopropanol (IPA) or flowing Ar gas showed a lower inhibition effect on 2-MBT degradation, suggesting the order of reactive species follows h$^+$ > $^\bullet O_2^-$ > $^\bullet$OH (Figure 2b). Additionally, the electron spin resonance (ESR) spectra directly show the existence of more h$^+$, $^\bullet O_2^-$, and $^\bullet$OH in the PCN−5B2T$_{100}$ D−π−A OCP system than in the PCN system (Figure 2c−e), matching well with the higher photocatalytic activity of PCN−5B2T$_{100}$ D−π−A OCP as compared to that of PCN. Furthermore, the PCN−5B2T$_{100}$ D−π−A OCP still possessed high photocatalytic activity after four continuous cycles of photodegradation reactions (Figures 2f and S17). Most importantly, PCN−5B2T$_{100}$ D−π−A OCP shows exceptional activity for photocatalytic 2-MBT degradation, far exceeding that of the other previously reported photocatalysts (Table S1).

Real-Time Analysis of the Intermediate Products over 2-MBT Degradation by the Fukui Function

To explore the photocatalytic degradation pathway of 2-MBT over PCN−5B2T$_{100}$ D−π−A OCP, the structural property of 2-MBT was investigated by DFT. As shown in Figure 3a−c, the C−H bond (C3, C4, and C6) has almost no contribution to the HOMO and LUMO orbitals, suggesting its weak reactivity. Figure 3d shows that the negatively charged surface is located at the S14 atom, pointing out that the S14 atom may be more prone to electron deprivation reactions. Therefore, the most vulnerable attack site in 2-MBT is located at the atom that contributes to the LUMO orbital due to the negatively charged surface electrostatic potential (ESP). To further analyze which atom will undergo electrophilic, nucleophilic, and radical attacks, Hirshfeld charges and the Fukui index (f^-, f^+, and f^0) were explored (Figure 3e−g). In general, $^\bullet$OH can not only act as an electrophilic species but also induce radical attack. h$^+$ and $^\bullet O_2^-$ possess certain electrophilicity and nucleophilicity, respectively.[43] As presented in Figure 3i, all atoms with higher values of f^-, f^+, and f^0 indicate that they are more easy to be attacked by $^\bullet O_2^-$, $^\bullet$OH, and h$^+$, respectively. Nevertheless, it is still difficult to accurately predict the reaction sites as the atom (S7) has both high electrophilicity and nucleophilicity. Therefore, we used the condensed dual descriptors (CDD) to define the reactive sites (Figure 3h).[44] Note that C3, C6, and C8 atoms show obvious nucleophilicity, while S14, S7, C4, and N9 atoms hold distinct electrophilicity in 2-MBT molecules, among which the S14 atom is the most active electrophilic sites, which can be easily attacked by h$^+$ and/or $^\bullet$OH to form P1 (m/z = 216) (Figures S18 and S19).

During the photodegradation reaction, the reaction sites of intermediates will vary due to structural changes. To monitor the structural changes of intermediates in real time, the structural properties of intermediates were investigated by the Fukui function. As shown in Figure S20a,c, the S10 and C8 atoms of the P1 molecule show relatively positive CDD values, which are easy to be attacked by $^\bullet O_2^-$ radicals, resulting in the fracture of the C−S bond in C−SO$_3$H to form P2 (m/z = 136). For the P2 molecule (Figure S20b−d), the C−S bond and C−N bond are easy to be attacked by h$^+$, $^\bullet O_2^-$, and $^\bullet$OH to generate P3 (m/z = 114). Successively, the further oxidation of P3 molecules leads to C−S and C−C bond breaking and hydroxylation to form P4 (m/z = 132), P5 (m/z = 60), and other small molecules (Figures S21 and S22). However, it is worth noting that only analyzing the active sites for possible degradation reactions of 2-MBT alone cannot truly reflect the degradation process. Therefore, the above Fukui function results that show the real-time structure change of 2-MBT are of great significance to reveal the overall degradation mechanism of 2-MBT under visible light irradiation. Additionally, the 3D EEM images further indicate that the 2-MBT molecules were gradually mineralized into other small organic molecules (Figure S23).

Efficient Light Absorption, Charge Separation, and Transfer Driven by D−π−A OCPs

To account for the greatly enhanced photocatalytic activity, the optical properties were investigated by DRS. Compared with PCN, the improved light absorption of PCN−5B2T$_x$ D−π−A OCPs is mainly due to the enhanced light scattering resulted from the holey structure and the narrowed band gap owing to the introduction of 5B2T (Figures S24 and S25). Besides, the finite-difference time-domain (FDTD) simulations also suggest that the holey PCN−5B2T$_x$ D−π−A OCPs possess stronger light absorption capacity (Figure S26). The bandgaps of PCN and PCN−5B2T$_{100}$ D−π−A OCP are estimated to be 2.58 and 1.75 eV, respectively. In addition, the flat-band potential (E_{FB}) values of PCN and PCN−5B2T$_{100}$ D−π−A OCP are determined at −1.41 and −1.10 V (vs Ag/AgCl, Figures S27 and S28), corresponding to −1.21 and −0.9 V (vs NHE), respectively. Note that PCN and PCN−5B2T$_x$ D−π−A OCPs display positive slopes in the Mott−Schottky plots, indicating n-type semiconductors.[45,46] Therefore, the minimum conduction band potentials of PCN and PCN−5B2T$_{100}$ D−π−A OCP are estimated to be −1.31 and −1.0 V (vs NHE, Figure S29), respectively. Compared with pure PCN, the density of states (DOS) indicates that the bandgaps of PCN−5B2T$_x$ D−π−A OCPs are markedly reduced (Figure S30a,b) due to the formation of new mid-gap (E_m) states induced by 5B2T, which extends the light absorption of PCN−5B2T$_x$ D−π−A OCPs to 1000 nm. For PCN, the HOMO and LUMO are mainly contributed by the nitrogen ρ_z orbitals and C−N orbitals, respectively (Figure S30c). However, α/β-HOMO and α/β-LUMO of PCN−5B2T$_x$ D−π−A OCPs are distributed on different structural units, indicating spatial separation of HOMO and LUMO. Furthermore, it is worth noting that there is no difference in the DOS of fragment 1, fragment 2, and fragment 3 of PCN, suggesting that each fragment of PCN contributes equally to the overall band

https://doi.org/10.1021/jacsau.3c00088
JACS Au 2023, 3, 1424−1434

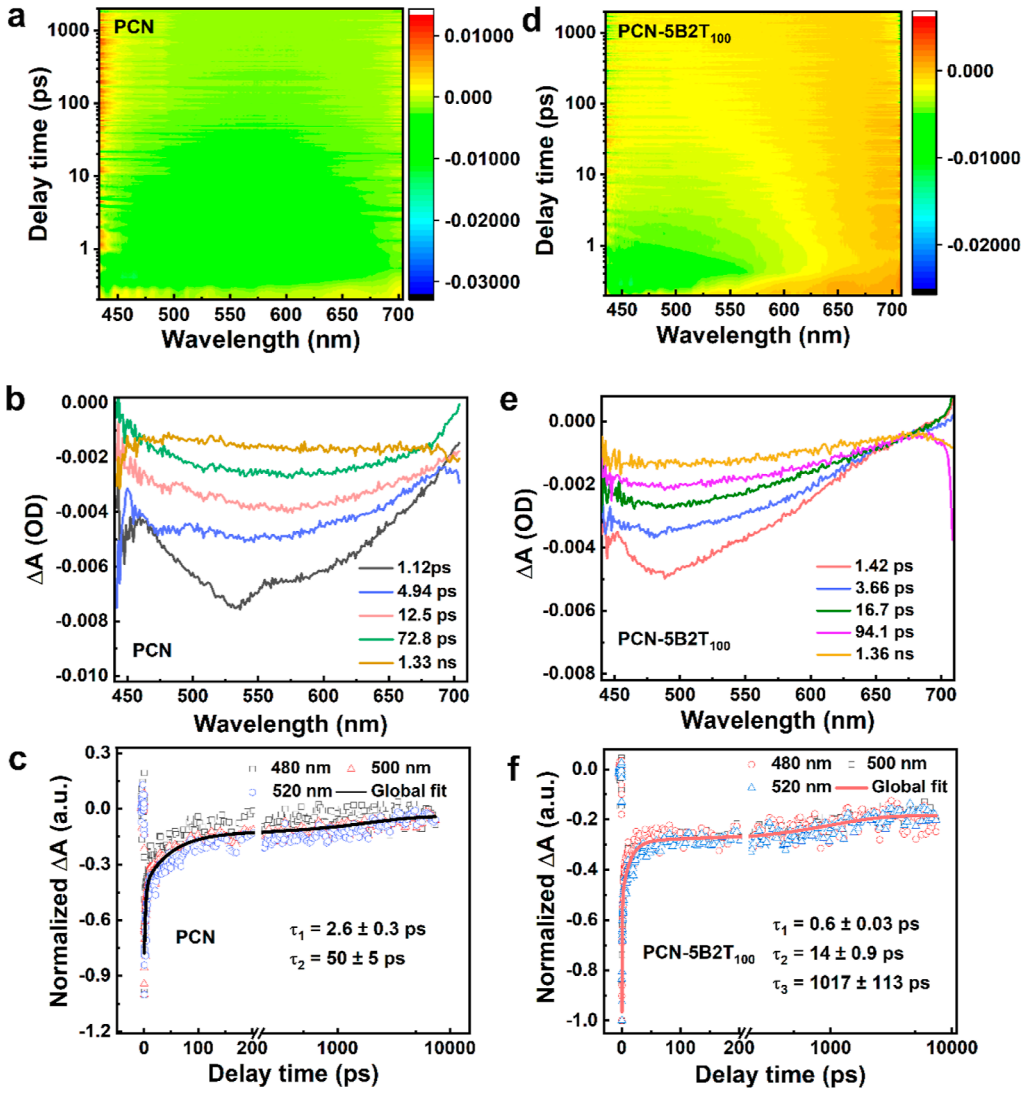

Figure 4. Contour plots of the time-resolved absorption spectroscopic responses and fs-TA spectra of (a,b) PCN and (d,e) PCN−5B2T$_{100}$ D−π−A OCP. The corresponding TA kinetics for (c) PCN and (f) PCN−5B2T$_{100}$ D−π−A OCP.

structure, which will result in low charge transfer efficiency. On the other hand, the DOSs of fragment 1, fragment 2, and fragment 3 of PCN−5B2T$_x$ D−π−A OCPs are very different, which is anticipated to improve the charge separation in PCN−5B2T$_x$ D−π−A OCPs.

To investigate the charge transfer/separation processes in PCN and PCN−5B2T$_x$ D−π−A OCPs, femtosecond transient absorption (fs-TA) spectroscopy was conducted. Both PCN (Figure 4a,b) and PCN−5B2T$_{100}$ D−π−A OCP (Figure 4d,e) show broadband characteristic peaks between 450 and 550 nm, respectively, which is due to the overlap between ground-state bleach and excited-state absorption signals.[47,48] In addition, a positive absorption band stemming from the excited-state absorption is observed in the fs-TA spectra of PCN−5B2T$_{100}$ D−π−A OCP, suggesting the presence of shallowly trapped electrons in PCN−5B2T$_{100}$ D−π−A OCP. For pure PCN, a two-exponential decay function was used to describe the carrier dynamics (Figure 4c). The decay lifetimes of τ_1 = 2.6 ± 0.3 ps and τ_2 = 50 ± 5 ps for PCN are assigned to electron transfer to the shallow trapping state and deep trapping state, respectively.[49] However, the intrinsic deep trapping state of pure PCN is induced by the insufficient extrinsic driving force in the photocatalyst, which would restrain the electron transfer.[50,51] Notably, eliminating the deeply trapped electrons or enhancing shallow trapping can improve the photocatalytic activity of PCN.[52] For PCN−5B2T$_{100}$ D−π−A OCP, it is interesting to note that a tri-exponential decay function was needed to fit the kinetics traces (Figure 4f). PCN−5B2T$_{100}$ D−π−A OCP introduces an electron acceptor relative to pure PCN, which will capture electrons faster. Therefore, the electrons are first transferred to the acceptor and then to the shallow trapping state. Correspondingly, the PCN−5B2T$_{100}$ D−π−A OCP possesses two fast decay components owing to the electron transfer to the trapping sites of the acceptor (τ_1 = 0.6 ± 0.03 ps) and to the shallow trapping state (τ_2 = 14 ± 0.9 ps). As expected, a longer decay lifetime of electron transfer to the shallow trapping state was obtained in PCN−5B2T$_{100}$ D−π−A OCP (14 ± 0.9 ps > 2.6 ± 0.3 ps of PCN), indicating the effectively strengthened shallow electron trapping. Additionally, τ_3 is an important time component to distinguish PCN with PCN−5B2T$_{100}$ D−π−A OCP in this work. The τ_3 (1017 ± 113 ps) for PCN−5B2T$_{100}$ D−π−A OCP shows the recombination of the shallow trapped electrons with holes.[53] That is to say, the τ_3 for PCN−5B2T$_{100}$ D−π−A OCP

https://doi.org/10.1021/jacsau.3c00088
JACS Au 2023, 3, 1424−1434

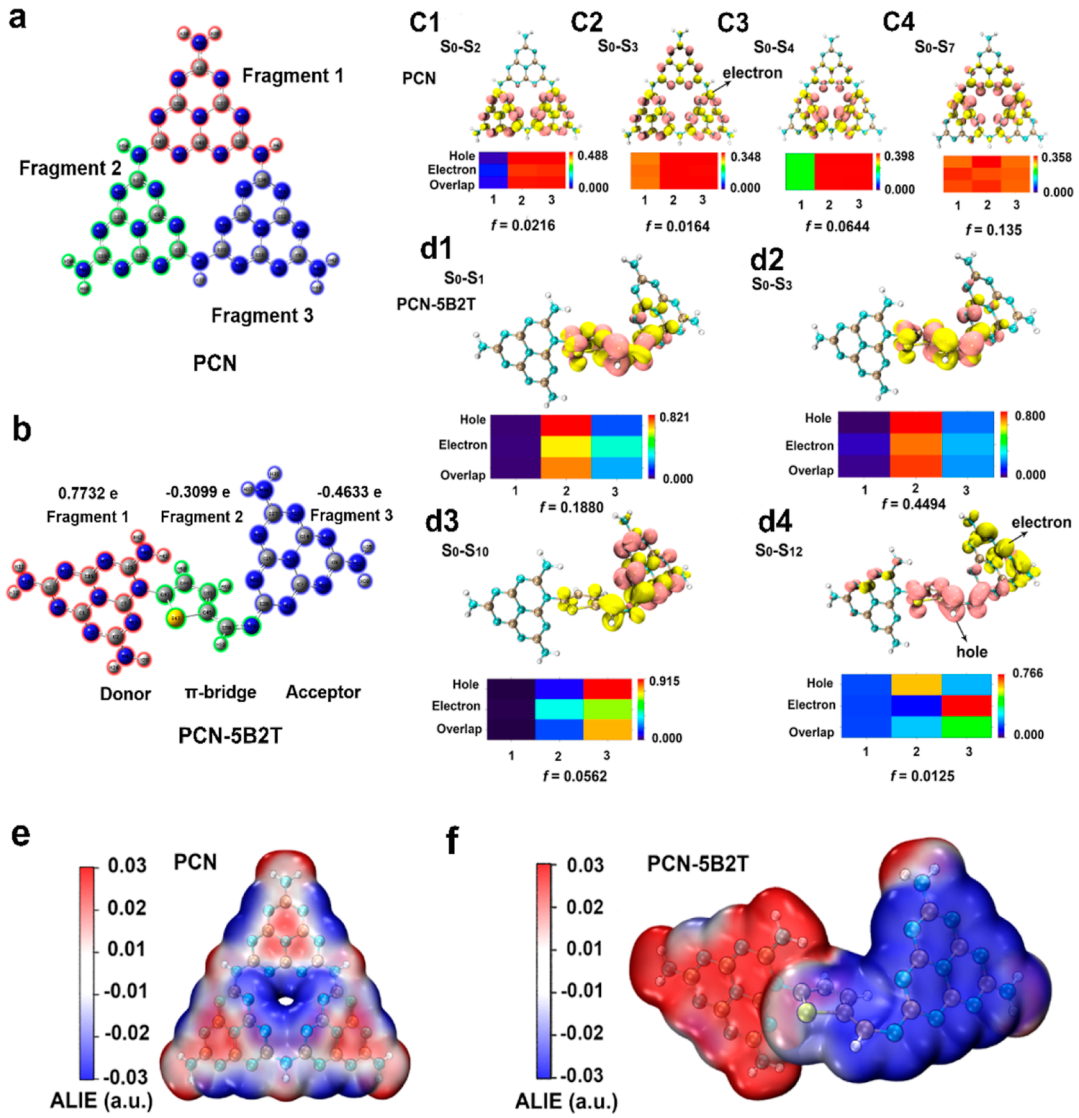

Figure 5. Excitation properties of PCN and PCN−5B2T D−π−A OCPs. The calculated Hirshfeld charges for (a) PCN and (b) PCN−5B2T$_x$ D−π−A OCPs. Electron−hole distribution of (c1−c4) PCN and (d1−d4) PCN−5B2T$_x$ D−π−A OCPs in different excited states. Yellow and pink isosurfaces represent electron and hole distributions, respectively. The isosurface value is 0.002 e/Å^3. ESP surface distribution of the optimized (e) PCN and (f) PCN−5B2T$_x$ D−π−A OCPs models.

represents the recombination of the shallow trapped electron with the hole on the HOMO. Figure S31 shows the schematic representation of the proposed charge trapping model in PCN and PCN−5B2T$_x$ D−π−A OCPs.[54] To further probe the spatial charge distribution, Kelvin probe force microscopy (KPFM) was performed.[55] Evidently, PCN−5B2T$_{100}$ D−π−A OCP displays much stronger surface photovoltage signals relative to PCN (Figure S32), demonstrating much faster separation and transport of photogenerated charge carriers in PCN−5B2T$_{100}$ D−π−A OCP. Besides, more efficient transfer and separation of charge carriers in PCN−5B2T$_{100}$ D−π−A OCP are also reflected by the shorter transient-state PL lifetime, higher photocurrent intensity, smaller arc radius, stronger EPR signal, and larger current density (Figures S33−S37).

To further study intramolecular charge transfer in PCN−5B2T$_x$ D−π−A OCPs, Hirshfeld charge analysis was performed by DFT. As shown in Figure 5b, fragment 1 of PCN−5B2T$_x$ D−π−A OCPs possesses a positive Hirshfeld charge of (0.7732 e), which explains their strong electron-donating ability.[56] Note that fragment 2 and fragment 3 show negative Hirshfeld charge values, suggesting that fragment 2 and fragment 3 can act as π-bridge and electron acceptor, respectively. Based on the Hirshfeld charge analysis, the electrons in PCN−5B2T$_x$ D−π−A OCPs as compared to those in PCN can be more easily transferred from the donor tertiary amine group to the benzene π-bridge and then to the acceptor imine group. To uncover the mechanism of electron excitation, the excited states of PCN and PCN−5B2T$_x$ D−π−A OCPs were calculated. As shown in Figure 5c,d, both PCN and PCN−5B2T$_x$ D−π−A OCPs have oscillator strengths greater than 0.01 (Tables S2 and S3), illustrating permittable transitions.[57] Figure 5c1−c4 shows poor charge separation in various excited states S0−S2, S0−S3, S0−S4, and S0−S7 of PCN. Compared to PCN, PCN−5B2T$_x$ D−π−A OCPs significantly accelerate the electron transfer in excited states S0−S1, S0−S3, and S0−S10 (Figure 5d1−d3). Noteworthily, electrons in PCN−5B2T$_x$ D−π−A OCPs are transferred from fragment 1 to fragment 2 and then to fragment 3 in excited states S0−S12 (Figure 5d4). In the meantime, holes are mainly

https://doi.org/10.1021/jacsau.3c00088
JACS Au 2023, 3, 1424−1434

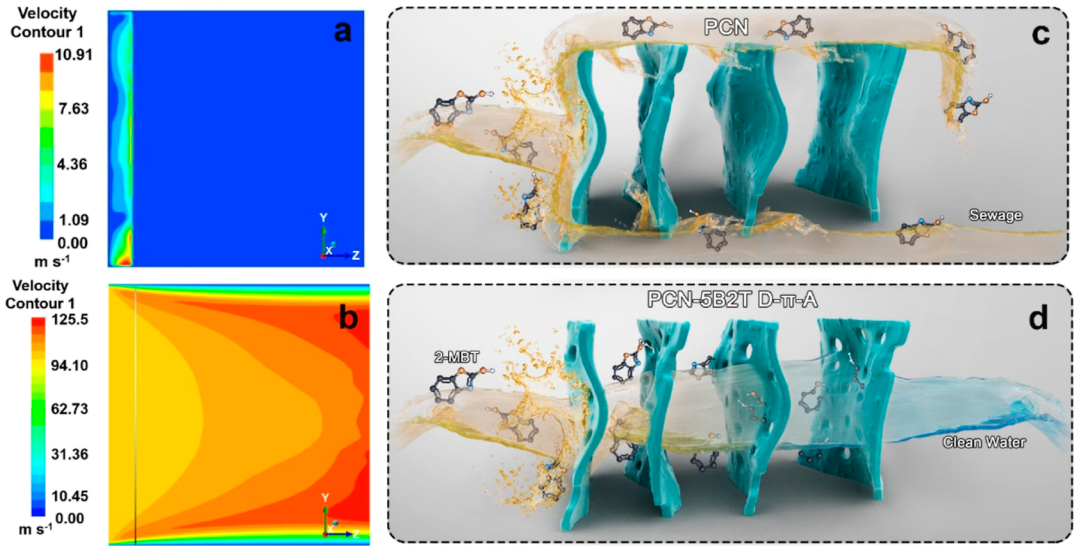

Figure 6. Velocity magnitude contours of water flow on (a) PCN and (b) PCN−5B2T$_x$ D−π−A OCPs. The mass transport diagram of 2-MBT on (c) PCN and (d) PCN−5B2T$_x$ D−π−A OCPs.

concentrated on the π-bridge, speculating that the π-bridge may be the main active site for h^+ to oxidize 2-MBT. Additionally, the simulated absorption spectra match well with the DRS results, revealing that the introduction of 5B2T into the PCN skeleton can effectively enhance light absorption (Figure 5e,f).

Mass Transfer Property of Holey D−π−A OCPs in the Degradation

Besides light absorption and the separation and transfer of charge carriers, mass transport also plays an important role in the photocatalytic degradation of 2-MBT. To evaluate the impact of different morphologies of bulk PCN and holey PCN−5B2T$_x$ D−π−A OCPs on mass transport, computational fluid dynamics (CFD) was investigated.[58] The velocity magnitude contours of the fluence are plotted in Figure 6a,b. It is interesting to find that the velocity of water in the holey PCN−5B2T$_x$ D−π−A OCPs reaches 125.5 m s^{-1}, nearly 11.5 times higher than that in PCN (10.91 m s^{-1}). The faster microfluidic flow in PCN−5B2T$_x$ D−π−A OCPs illustrates that the holey structure is indeed beneficial to mass transport. Based on the above analysis, the mass transport of 2-MBT in PCN and holey PCN−5B2T$_x$ D−π−A OCPs are compared. As illustrated in Figure 6c, PCN exhibits poor mass transport, which limits its photocatalytic activity. On the other hand, the holey structure of PCN−5B2T$_x$ D−π−A OCPs significantly improves the mass transport of 2-MBT (Figure 6d) and thus enhances the efficiency for 2-MBT degradation. In addition, PCN−5B2T$_x$ D−π−A OCPs display stronger adsorption of 2-MBT at the donor and π-bridge sites than the acceptor sites (Figure S38). Together with the fact that photogenerated holes tend to accumulate on the π-bridge, the π-bridge sites are most likely the main active sites for photodegradation of 2-MBT. With the above analyses, the possible mechanism and the underlying reasons for the greatly enhanced photocatalytic activity toward 2-MBT degradation on PCN−5B2T$_x$ D−π−A COPs are summarized in Figures S39 and S40. Overall speaking, PCN−5B2T$_x$ D−π−A COPs have the following advantages over PCN: (i) introducing π-bridge into PCN−5B2T significantly enhanced the separation efficiency of charge carriers; (ii) π-bridge sites not only significantly enhanced the selective adsorption ability for 2-MBT but also enriched the major active species (photo-generated holes) of 2-MBT degradation; (iii) PCN−5B2T$_x$ D−π−A COPs produced new midgap states, which could obviously expand the light absorption range; and (iv) the holey structure of PCN−5B2T$_x$ D−π−A COPs effectively promoted mass transport.

CONCLUSIONS

In summary, holey metal-free PCN−5B2T$_x$ D−π−A OCPs have been successfully designed and synthesized by copolymerizing urea and 5B2T based on nucleophilic substitution and Schiff base chemical reactions. Experimental and DFT calculation results show that the obtained PCN−5B2T$_{100}$ D−π−A OCPs not only increased the specific surface area and improved light absorption but also enhanced the intramolecular charge transfer. Meanwhile, the CFD results also demonstrated that the holey PCN−5B2T$_x$ D−π−A OCPs were beneficial to mass transport. As a result, the PCN−5B2T$_{100}$ D−π−A OCP exhibited outstanding photocatalytic activity toward the degradation of 2-MBT, which is ∼10 times higher than that of PCN. Furthermore, the real-time reaction process for the degradation of 2-MBT was analyzed by the Fukui function. The π-bridge was found to accumulate photogenerated holes as well as adsorb 2-MBT molecules, which thus acted as the active sites for photodegradation of 2-MBT. Building D−π−A OCPs with holey structures provides an effective strategy to design highly efficient photocatalysts for energy conversion and environmental remediation.

EXPERIMENTAL SECTION

Preparation of PCN−5B2T D−π−A OCPs

PCN−5B2T D−π−A OCPs were prepared by nucleophilic substitution and Schiff base chemical reaction through polycondensation of urea and 5B2T. The details are summarized as follows: 20 g of urea was placed in a beaker and heated to 160 °C in an oil bath under stirring until melted completely. Afterward, a certain amount of 5B2T was added to the above molten urea and continuously stirred for 20 min to obtain a uniform mixture. The mixture was recrystallized at room temperature and quickly transferred to a muffle furnace for calcination (550 °C for 3 h at a heating rate of 5 °C/min). The obtained samples are denoted as PCN−5B2T$_x$ (x = 10, 100, and 200)

https://doi.org/10.1021/jacsau.3c00088
JACS Au 2023, 3, 1424−1434

D−π−A OCPs, in which "x" indicates the volume (μL) of the added 5B2T. For comparison, bulk PCN was synthetized by a similar process except that 5B2T was not added.

Photocatalytic Degradation of 2-MBT

2-Mercaptobenzothiazole (2-MBT), a typical heterocyclic compound, has been extensively used as a fungicide in all kinds of consumer products and as vulcanization accelerators in rubber manufacturing. Especially 2-MBT is widely used in rubber pipe parts in contact with drinking water, which causes severe damage to aquatic organisms and human health. The photocatalytic activities of PCN and PCN−5B2T D−π−A OCPs were estimated by degradation of 2-MBT under visible light irradiation (300 W Xe lamp with $\lambda > 420$ nm). First, 25 mg of the as-prepared catalyst was dispersed in 50 mL (10 mg/L) of 2-MBT aqueous solution. Then, the suspension was magnetically stirred in the dark for 30 min to reach adsorption−desorption equilibrium. During the illumination process, 1.5 mL of the suspension was extracted every 2 min. The temperature of the whole reaction system was maintained at 25 °C by condensation water. The withdrawn suspension was centrifuged and filtered by a 0.22 μm filter. Afterward, the filtered solution of 2-MBT was analyzed by a Shimadzu UV-3600 spectrofluorometer.

■ ASSOCIATED CONTENT

Supporting Information

The Supporting Information is available free of charge at https://pubs.acs.org/doi/10.1021/jacsau.3c00088.

Experimental section; SEM and TEM images of PCN and PCN−5B2T$_x$ D−π−A OCPs; BET, XRD, FT-IR, XPS, solid-state ^{13}C NMR, and MALDI-TOF MS spectra of PCN and PCN−5B2T D−π−A OCPs; adsorption/desorption equilibrium of as-prepared samples; photocatalytic degradation kinetics of 2-MBT over PCN and PCN−5B2T D−π−A OCPs; 3D EEMs, UV−vis diffuse reflectance spectra, distribution of electrical field, and Mott−Schottky plots of PCN and PCN−5B2T$_x$ D−π−A OCPs; photoelectric properties (photocurrent density and EIS) of as-prepared samples; and DFT calculation (PDF)

■ AUTHOR INFORMATION

Corresponding Authors

Yanhui Ao − *Key Laboratory of Integrated Regulation and Resource Development on Shallow Lakes, Ministry of Education, College of Environment, Hohai University, Nanjing 210098, China;* orcid.org/0000-0002-3665-9881; Email: andyao@hhu.edu.cn

Bin Liu − *Department of Materials Science and Engineering, City University of Hong Kong, Hong Kong-SAR 999077, China;* orcid.org/0000-0002-4685-2052; Email: bliu48@cityu.edu.hk

Authors

Huinan Che − *Key Laboratory of Integrated Regulation and Resource Development on Shallow Lakes, Ministry of Education, College of Environment, Hohai University, Nanjing 210098, China*

Jian Wang − *Key Laboratory of Integrated Regulation and Resource Development on Shallow Lakes, Ministry of Education, College of Environment, Hohai University, Nanjing 210098, China*

Peifang Wang − *Key Laboratory of Integrated Regulation and Resource Development on Shallow Lakes, Ministry of Education, College of Environment, Hohai University, Nanjing 210098, China;* orcid.org/0000-0003-3010-1008

Juan Chen − *Key Laboratory of Integrated Regulation and Resource Development on Shallow Lakes, Ministry of Education, College of Environment, Hohai University, Nanjing 210098, China*

Xin Gao − *Key Laboratory of Integrated Regulation and Resource Development on Shallow Lakes, Ministry of Education, College of Environment, Hohai University, Nanjing 210098, China*

Fangyuan Zhu − *Shanghai Synchrotron Radiation Facility, Shanghai Advanced Research Institute, Chinese Academy of Sciences, Shanghai 201204, China*

Complete contact information is available at: https://pubs.acs.org/10.1021/jacsau.3c00088

Author Contributions

H.C. and J.W. contributed equally to this work. All authors have given approval to the final version of the manuscript. CRediT: H.C.: data curation, investigation, and writing-original draft; J.W.: data curation, formal analysis, investigation, and writing-review and editing; P.W.: formal analysis, investigation, and writing-review and editing; J.C.: formal analysis, investigation, and writing-review and editing; X.G.: DFT theoretical calculation and data analysis; F.Z.: assistance with XMCD/XAFS data collection. Y.A. and B.L.: conceptualization, formal analysis, funding acquisition, resources, supervision, and writing-review and editing.

Notes

The authors declare no competing financial interest.

■ ACKNOWLEDGMENTS

We are grateful for the grants from the Natural Science Foundation of China (nos. 51979081 and 52100179), the Fundamental Research Funds for the Central Universities (no. B210202052), the China Postdoctoral Science Foundation (nos. 2020M680063 and 2021T140176), the City University of Hong Kong start-up fund, and PAPD. We thank the staff from the BL07U beamline of the Shanghai Synchrotron Radiation Facility (SSRF) for their assistance with XMCD/XAFS data collection.

■ REFERENCES

(1) Yang, M. Q.; Gao, M. M.; Hong, M. H.; Ho, G. W. Visible-to-NIR photon harvesting: progressive engineering of catalysts for solar-powered environmental purification and fuel production. *Adv. Mater.* **2018**, *30*, 1802894.

(2) Shiraishi, Y.; Kanazawa, S.; Sugano, Y.; Tsukamoto, D.; Sakamoto, H.; Ichikawa, S.; Hirai, T. Highly selective production of hydrogen peroxide on graphitic carbon nitride (g-C_3N_4) photocatalyst activated by visible light. *ACS Catal.* **2014**, *4*, 774−780.

(3) Ji, L. T.; Yan, L. K.; Chao, M.; Li, M. R.; Gu, J. C.; Lei, M.; Zhang, Y. M.; Wang, X.; Xia, J. Y.; Chen, T. Y.; Nie, Y. J.; Chen, T. Sphagnum inspired g-C_3N_4 nano/microspheres with smaller bandgap in heterojunction membranes for sunlight-driven water purification. *Small* **2021**, *17*, 2007122.

(4) Fu, J. W.; Yu, J. G.; Jiang, C. J.; Cheng, B. g-C_3N_4-based heterostructured photocatalysts. *Adv. Energy Mater.* **2018**, *8*, 1701503.

(5) Liao, G. F.; Gong, Y.; Zhang, L.; Gao, H. Y.; Yang, G. J.; Fang, B. Z. Semiconductor polymeric graphitic carbon nitride photocatalysts: the "holy grail" for the photocatalytic hydrogen evolution reaction under visible light. *Energy Environ. Sci.* **2019**, *12*, 2080−2147.

(6) Zhang, L. S.; Jiang, X. H.; Zhong, Z. A.; Tian, L.; Sun, Q.; Cui, Y. T.; Lu, X.; Zou, J. P.; Luo, S. L. Carbon nitride supported high-loading Fe single-atom catalyst for activation of peroxymonosulfate to generate $^1O_2$ with 100% selectivity. *Angew. Chem., Int. Ed.* **2021**, *60*, 21751−21755.
(7) Zhao, Y.; Zhang, P.; Yang, Z.; Li, L.; Gao, J.; Chen, S.; Xie, T.; Diao, C.; Xi, S.; Xiao, B.; Hu, C.; Choi, W. Mechanistic analysis of multiple processes controlling solar-driven H_2O_2 synthesis using engineered polymeric carbon nitride. *Nat. Commun.* **2021**, *12*, 3701.
(8) Jiang, X. H.; Zhang, L. S.; Liu, H. Y.; Wu, D. S.; Wu, F. Y.; Tian, L.; Liu, L. L.; Zou, J. P.; Luo, S. L.; Chen, B. B. Silver single atom in carbon nitride catalyst for highly efficient photocatalytic hydrogen evolution. *Angew. Chem., Int. Ed.* **2020**, *59*, 23112−23116.
(9) Deng, Y. C.; Liu, J.; Huang, Y. B.; Ma, M. M.; Liu, K.; Dou, X. M.; Wang, Z. J.; Qu, S. C.; Wang, Z. G. Engineering the photocatalytic behaviors of g/C_3N_4-based metal-free materials for degradation of a representative antibiotic. *Adv. Funct. Mater.* **2020**, *30*, 2002353.
(10) Xu, J.; Wang, Z. P.; Zhu, Y. F. Enhanced visible-light-driven photocatalytic disinfection performance and organic pollutant degradation activity of holey g-C_3N_4 nanosheets. *ACS Appl. Mater. Interfaces* **2017**, *9*, 27727−27735.
(11) Lau, V. W.; Moudrakovski, I.; Botari, T.; Weinberger, S.; Mesch, M. B.; Duppel, V.; Senker, J.; Blum, V.; Lotsch, B. V. Rational design of carbon nitride photocatalysts by identification of cyanamide defects as catalytically relevant sites. *Nat. Commun.* **2016**, *7*, 12165.
(12) Xiong, Y.; Chen, Y. P.; Yang, N.; Jin, C. D.; Sun, Q. F. WC_{1-x}-coupled 3D holey defective g-C_3N_4 for efficient photocatalytic overall water splitting. *Sol. RRL* **2019**, *3*, 1800341.
(13) Zhao, D. M.; Dong, C. L.; Wang, B.; Chen, C.; Huang, Y. C.; Diao, Z. D.; Li, S. Z.; Guo, L. J.; Shen, S. H. Synergy of dopants and defects in graphitic carbon nitride with exceptionally modulated band structures for efficient photocatalytic oxygen evolution. *Adv. Mater.* **2019**, *31*, 1903545.
(14) Yu, X. N.; Ng, S. F.; Putri, L. K.; Tan, L. L.; Mohamed, A. R.; Ong, W. Point-defect engineering: leveraging imperfections in graphitic carbon nitride (g-C_3N_4) photocatalysts toward artificial photosynthesis. *Small* **2021**, *17*, 2006851.
(15) Chu, X. Y.; Qu, Y.; Zada, A.; Bai, L. L.; Li, Z. J.; Yang, F.; Zhao, L. N.; Zhang, G. L.; Sun, X. J.; Yang, Z. D.; Jing, L. Q. Ultrathin phosphate-modulated Co phthalocyanine/g-C_3N_4 heterojunction photocatalysts with single Co-N_4 (II) sites for efficient O_2 activation. *Adv. Sci.* **2020**, *7*, 2001543.
(16) Guo, S. Q.; Zhang, H. J.; Hu, Z. Z.; Zhen, M. M.; Yang, B.; Shen, B. X.; Dong, F. Composition-dependent micro-structure and photocatalytic performance of g-C_3N_4 quantum dots@SnS_2 heterojunction. *Nano Res.* **2021**, *14*, 4188−4196.
(17) Wang, Q. L.; Wang, X. K.; Yu, Z. H.; Jiang, X. X.; Chen, J. J.; Tao, L. M.; Wang, M. K.; Shen, Y. Artificial photosynthesis of ethanol using type-II g-C_3N_4/ZnTe heterojunction in photoelectrochemical CO_2 reduction system. *Nano Energy* **2019**, *60*, 827−835.
(18) Yang, Q.; Yu, S. W.; Fu, P.; Yu, W.; Liu, Y.; Liu, X.; Feng, Z. C.; Guo, X.; Li, C. Boosting performance of non-fullerene organic solar cells by 2D g-C_3N_4 doped PEDOT: PSS. *Adv. Funct. Mater.* **2020**, *30*, 1910205.
(19) Chu, Y. C.; Lin, T. J.; Lin, Y. R.; Chiu, W. L.; Nguyen, B. S.; Hu, C. C. Influence of P, S, O-doping on g-C_3N_4 for hydrogel formation and photocatalysis: an experimental and theoretical study. *Carbon* **2020**, *169*, 338−348.
(20) Hu, C. C.; Wang, M. S.; Chen, C. H.; Chen, Y. R.; Huang, P. H.; Tung, K. L. Phosphorus-doped g-C_3N_4 integrated photocatalytic membrane reactor for wastewater treatment. *J. Membr. Sci.* **2019**, *580*, 1−11.
(21) Barman, S.; Singh, A.; Rahimi, F. A.; Maji, T. K. Metal-free catalysis: a redox-active donor-acceptor conjugated microholey polymer for selective visible-light-driven CO_2 reduction to CH_4. *J. Am. Chem. Soc.* **2021**, *143*, 16284−16292.
(22) Chen, J.; Dong, C. L.; Zhao, D. M.; Huang, Y. C.; Wang, X. X.; Samad, L.; Dang, L.; Shearer, M.; Shen, S.; Guo, L. Molecular design of polymer heterojunctions for efficient solar-hydrogen conversion. *Adv. Mater.* **2017**, *29*, 1606198.
(23) Hashemi, D.; Ma, X.; Ansari, R.; Kim, J.; Kieffer, J. Design principles for the energy level tuning in donor/acceptor conjugated polymers. *Phys. Chem. Chem. Phys.* **2019**, *21*, 789−799.
(24) Zhao, W. L.; Zhai, D.; Liu, C. C.; Zheng, D. Y.; Wu, H.; Sun, L.; Li, Z.; Yu, T.; Zhou, W.; Fang, X.; Zhai, S. L.; Han, K. L.; He, Z. L.; Deng, W. Q. Unblocked intramolecular charge transfer for enhanced CO_2 photoreduction enabled by an imidazolium-based ionic conjugated microholey polymer. *Appl. Catal., B* **2022**, *300*, 120719.
(25) Han, C. Z.; Xiang, S. H.; Jin, S. L.; Zhang, C.; Jiang, J. X. Rational design of conjugated microporous polymer photocatalysts with definite D−π−A structures for ultrahigh photocatalytic hydrogen evolution activity under natural sunlight. *ACS Catal.* **2023**, *13*, 204−212.
(26) Han, C. Z.; Xiang, S. H.; Xie, P. X.; Dong, P. H.; Shu, C.; Zhang, C.; Jiang, J. X. A universal strategy for boosting hydrogen evolution activity of polymer photocatalysts under visible light by inserting a narrow-band-gap spacer between donor and acceptor. *Adv. Funct. Mater.* **2022**, *32*, 2109423.
(27) Che, W.; Cheng, W. R.; Yao, T.; Tang, F.; Liu, W.; Su, H.; Huang, Y.; Liu, Q.; Liu, J.; Hu, F.; Pan, Z.; Sun, Z. Fast photoelectron transfer in (C_{ring})-C_3N_4 plane heterostructural nanosheets for overall water splitting. *J. Am. Chem. Soc.* **2017**, *139*, 3021−3026.
(28) Li, Y. F.; Wang, S.; Chang, W.; Zhang, L. H.; Wu, Z. S.; Jin, R. X.; Xing, Y. Co-monomer engineering optimized electron delocalization system in carbon-bridging modified g-C_3N_4 nanosheets with efficient visible-light photocatalytic performance. *Appl. Catal., B* **2020**, *274*, 119116.
(29) Shao, C. F.; Zhuang, S. G.; Zhang, H. C.; Jiang, Q. K.; Xu, X. Y.; Ye, J. S.; Li, B. T.; Wang, X. J. Enhancement of Mass Transport for Oxygen Reduction Reaction Using Petal-Like Porous Fe-NC Nanosheet. *Small* **2021**, *17*, 2006178.
(30) Teng, Z. Y.; Zhang, Q. T.; Yang, H. B.; Kato, K.; Yang, W. J.; Lu, Y. R.; Liu, S. X.; Wang, C. Y.; Yamakata, A.; Su, C. L.; Liu, B.; Ohno, T. Atomically dispersed antimony on carbon nitride for the artificial photosynthesis of hydrogen peroxide. *Nat. Catal.* **2021**, *4*, 374−384.
(31) Che, H. N.; Gao, X.; Chen, J.; Hou, J.; Ao, Y. H.; Wang, P. F. Iodide-induced fragmentation of polymerized hydrophilic carbon nitride for high-performance quasi-homogeneous photocatalytic H_2O_2 production. *Angew. Chem., Int. Ed.* **2021**, *60*, 25546.
(32) Zhang, X.; Ma, P. J.; Wang, C.; Gan, L. Y.; Chen, X. J.; Zhang, P.; Wang, Y.; Li, H.; Wang, L. H.; Zhou, X. Y.; Zheng, K. Unraveling the dual defect sites in graphite carbon nitride for ultra-high photocatalytic H_2O_2 evolution. *Energy Environ. Sci.* **2022**, *15*, 830−842.
(33) Wang, Y.; Du, P. P.; Pan, H. Z.; Fu, L.; Zhang, Y.; Chen, J.; Du, Y. W.; Tang, N. J.; Liu, G. Increasing solar absorption of atomically thin 2D carbon nitride sheets for enhanced visible-light photocatalysis. *Adv. Mater.* **2019**, *31*, 1807540.
(34) Dong, H. J.; Xiao, M. Y.; Yu, S. Y.; Wu, H. H.; Wang, Y.; Sun, J. X.; Chen, G.; Li, C. M. Insight into the activity and stability of Rh_xP nano-species supported on g-C_3N_4 for photocatalytic H_2 production. *ACS Catal.* **2020**, *10*, 458−462.
(35) Zhang, P.; Sun, D. R.; Cho, A.; Weon, S.; Lee, S.; Lee, J.; Han, J. W.; Kim, D. P.; Choi, W. Modified carbon nitride nanozyme as bifunctional glucose oxidase-peroxidase for metal-free bioinspired cascade photocatalysis. *Nat. Commun.* **2019**, *10*, 940.
(36) Li, K.; Wang, L.; Chen, Z. X.; Yang, X. F.; Yu, Y. X.; Zhang, W. D.; Wang, Y.; Shi, Y. M.; Loh, K. P.; Xu, Q. H. Photocatalytic hydrogen evolution under ambient conditions on polymeric carbon nitride/donor-π-acceptor organic molecule heterostructures. *Adv. Funct. Mater.* **2020**, *30*, 2005106.
(37) Borrelli, M.; Querebillo, C. J.; Pastoetter, D. L.; Wang, T.; Milani, A.; Casari, C.; Khoa Ly, H.; He, F.; Hou, Y.; Neumann, C.; Turchanin, A.; Sun, H.; Weidinger, I. M.; Feng, X. Thiophene-based conjugated acetylenic polymers with dual active sites for efficient co-

https://doi.org/10.1021/jacsau.3c00088
JACS Au 2023, 3, 1424−1434

catalyst-free photoelectrochemical water reduction in alkaline medium. *Angew. Chem., Int. Ed.* **2021**, *60*, 18876−18881.
(38) Zhou, Y.; Lv, W. H.; Zhu, B. L.; Tong, F.; Pan, J. L.; Bai, J. R.; Zhou, Q. F.; Qin, H. F. Template-free one-step synthesis of g-C_3N_4 nanosheets with simultaneous porous network and S-doping for remarkable visible-light-driven hydrogen evolution. *ACS Sustainable Chem. Eng.* **2019**, *7*, 5801−5807.
(39) Yang, C.; Wang, B.; Zhang, L.; Yin, L.; Wang, X. Synthesis of layered carbonitrides from biotic molecules for photoredox transformations. *Angew. Chem., Int. Ed.* **2017**, *56*, 6627−6631.
(40) Xu, S. Q.; Sun, H. J.; Addicoat, M.; Biswal, B. P.; He, F.; Park, S. W.; Paasch, S.; Zhang, T.; Sheng, W. B.; Brunner, E.; Hou, Y.; Richter, M.; Feng, X. L. Thiophene-bridged donor-acceptor sp2-carbon-linked 2D conjugated polymers as photocathodes for water reduction. *Adv. Mater.* **2021**, *33*, 2006274.
(41) Ou, H. H.; Chen, X. R.; Lin, L. H.; Fang, Y. X.; Wang, X. C. Biomimetic donor-acceptor motifs in conjugated polymers for promoting exciton splitting and charge separation. *Angew. Chem., Int. Ed.* **2018**, *57*, 8729−8733.
(42) Mo, Z.; Di, J.; Yan, P. C.; Lv, C. D.; Zhu, X. W.; Liu, D. B.; Song, Y. H.; Liu, C. T.; Yu, Q.; Li, H. M.; Lei, Y. C.; Xu, H.; Yan, Q. Y. An all-organic D-A system for visible-light-driven overall water splitting. *Small* **2020**, *16*, 2003914.
(43) Liu, W.; Li, Y. Y.; Liu, F. Y.; Jiang, W.; Zhang, D. D.; Liang, J. L. Visible-light-driven photocatalytic degradation of diclofenac by carbon quantum dots modified holey g-C_3N_4: mechanisms, degradation pathway and DFT calculation. *Water Res.* **2019**, *151*, 8−19.
(44) Ji, H. D.; Du, P. H.; Zhao, D. Y.; Li, S.; Sun, F. B.; Duin, E. C.; Liu, W. 2D/1D graphitic carbon nitride/titanate nanotubes heterostructure for efficient photocatalysis of sulfamethazine under solar light: catalytic "hot spots" at the rutile-anatase-titanate interfaces. *Appl. Catal., B* **2020**, *263*, 118357.
(45) Yu, H. J.; Chen, F.; Li, X. W.; Huang, H. W.; Zhang, Q. Y.; Su, S. Q.; Wang, K. Y.; Mao, E. Y.; Mei, B.; Mul, G.; Ma, T. Y.; Zhang, Y. H. Synergy of ferroelectric polarization and oxygen vacancy to promote CO_2 photoreduction. *Nat. Commun.* **2021**, *12*, 4594.
(46) Vidyasagar, D.; Ghugal, S. G.; Banavoth, M. Extended π-conjugative np type homostructural graphitic carbon nitride for photodegradation and charge-storage applications. *Sci. Rep.* **2019**, *9*, 7186.
(47) Corp, K. L.; Schlenker, C. W. Ultrafast spectroscopy reveals electron-transfer cascade that improves hydrogen evolution with carbon nitride photocatalysts. *J. Am. Chem. Soc.* **2017**, *139*, 7904−7912.
(48) Lei, W.; Mi, Y.; Feng, R.; Liu, P.; Hu, S.; Yu, J.; Liu, X.; Rodriguez, J. A.; Wang, J. O.; Zheng, L.; Tang, K.; Zhu, S.; Liu, G.; Liu, M. Hybrid 0D-2D black phosphorus quantum dots-graphitic carbon nitride nanosheets for efficient hydrogen evolution. *Nano Energy* **2018**, *50*, 552−561.
(49) Qian, M. Y.; Wu, X. L.; Lu, M.; Huang, L. Z.; Li, W. X.; Lin, H. J.; Chen, J. R.; Wang, S. B.; Duan, X. G. Modulation of charge trapping by island-like single-atom cobalt catalyst for enhanced photo-fenton-like reaction. *Adv. Funct. Mater.* **2023**, *33*, 2208688.
(50) Jing, L.; Zhu, R. X.; Phillips, D. L.; Yu, J. C. Effective prevention of charge trapping in graphitic carbon nitride with nanosized red phosphorus modification for superior photo(electro)catalysis. *Adv. Funct. Mater.* **2017**, *27*, 1703484.
(51) Godin, R.; Wang, Y.; Zwijnenburg, M. A.; Tang, J. W.; Durrant, J. R. Time-resolved spectroscopic investigation of charge trapping in carbon nitrides photocatalysts for hydrogen generation. *J. Am. Chem. Soc.* **2017**, *139*, 5216−5224.
(52) Wang, W.; Tao, Y.; Du, L.; Wei, Z.; Yan, Z.; Chan, W. K.; Lian, Z.; Zhu, R.; Phillips, D. L.; Li, G. Femtosecond time-resolved spectroscopic observation of long-lived charge separation in bimetallic sulfide/g-C_3N_4 for boosting photocatalytic H_2 evolution. *Appl. Catal., B* **2021**, *282*, 119568.
(53) Cheng, C.; Zhang, J.; Zhu, B.; Liang, G.; Zhang, L.; Yu, J. Verifying the charge-transfer mechanism in S-Scheme heterojunctions using femtosecond transient absorption spectroscopy. *Angew. Chem., Int. Ed.* **2023**, *62*, 202218688.
(54) Wang, W. C.; Tao, Y.; Fan, J. C.; Yan, Z. P.; Shang, H.; Phillips, D. L.; Chen, M.; Li, G. S. Fullerene−graphene acceptor drives ultrafast carrier dynamics for sustainable CdS photocatalytic hydrogen evolution. *Adv. Funct. Mater.* **2022**, *32*, 2201357.
(55) Wang, X. D.; Huang, Y. H.; Liao, J. F.; Jiang, Y.; Zhou, L.; Zhang, X. Y.; Chen, H. Y.; Kuang, D. B. In situ construction of a Cs_2SnI_6 perovskite nanocrystal/SnS_2 nanosheet heterojunction with boosted interfacial charge transfer. *J. Am. Chem. Soc.* **2019**, *141*, 13434−13441.
(56) Yu, F. T.; Wang, Z. Q.; Zhang, S. C.; Ye, H. N.; Kong, K. Y.; Gong, X. Q.; Hua, J. L.; Tian, H. Molecular engineering of donor-acceptor conjugated polymer/g-C_3N_4 heterostructures for significantly enhanced hydrogen evolution under visible-light irradiation. *Adv. Funct. Mater.* **2018**, *28*, 1804512.
(57) Adamo, C.; Jacquemin, D. The calculations of excited-state properties with time-dependent density functional theory. *Chem. Soc. Rev.* **2013**, *42*, 845−856.
(58) Song, R.; Chi, H. B.; Ma, Q. L.; Li, D. F.; Wang, X. M.; Gao, W. S.; Wang, H.; Wang, X. L.; Li, Z. L.; Li, C. Highly efficient degradation of persistent pollutants with 3D nanocone TiO_2-based photoelectrocatalysis. *J. Am. Chem. Soc.* **2021**, *143*, 13664−13674.

https://doi.org/10.1021/jacsau.3c00088
JACS Au 2023, 3, 1424−1434